BIOENGINEERING

Harnessing the hygroscopic and biofluorescent behaviors of genetically tractable microbial cells to design biohybrid wearables

Wen Wang,[1,2] Lining Yao,[2] Chin-Yi Cheng,[2,3] Teng Zhang,[4] Hiroshi Atsumi,[5] Luda Wang,[4] Guanyun Wang,[2] Oksana Anilionyte,[2] Helene Steiner,[2] Jifei Ou,[2] Kang Zhou,[6] Chris Wawrousek,[7] Katherine Petrecca,[7] Angela M. Belcher,[5] Rohit Karnik,[4] Xuanhe Zhao,[4]* Daniel I. C. Wang,[1]* Hiroshi Ishii[2]*

Cells' biomechanical responses to external stimuli have been intensively studied but rarely implemented into devices that interact with the human body. We demonstrate that the hygroscopic and biofluorescent behaviors of living cells can be engineered to design biohybrid wearables, which give multifunctional responsiveness to human sweat. By depositing genetically tractable microbes on a humidity-inert material to form a heterogeneous multilayered structure, we obtained biohybrid films that can reversibly change shape and biofluorescence intensity within a few seconds in response to environmental humidity gradients. Experimental characterization and mechanical modeling of the film were performed to guide the design of a wearable running suit and a fluorescent shoe prototype with bio-flaps that dynamically modulates ventilation in synergy with the body's need for cooling.

INTRODUCTION

In nature, the basic units of life are cells, which can dynamically adjust their behaviors biochemically (*1*) or biomechanically (*2*) in response to signals indicating environmental change, such as nutrient levels (*3*), shear stress (*4*), and electrical pulses (*5*). Among those stimuli, the moisture gradient is an intriguing factor, which can trigger shape transformation in plant due to mechanical amplification of moisture-induced strains in hygroscopic tissues [for example, pine cone scales (*6*) and wheat awns (*7*)]. Inspired by this hygroscopic information-processing concept (*8*), researchers previously developed active materials with unique geometric constraints or structural heterogeneities, including polymers for fabricating hygrovoltaic generators (*9*), hydrogels for forming complex micropatterns (*10*), spores for harvesting energy (*11*), and wood for building innovative pavilions (*12*). These previous studies primarily focused on innovative applications by using nonliving materials, the chemical performance and mechanical performance of which are predefined before fabrication. For instance, spores or harvested wood materials are not biologically active and are insusceptible to direct genetic engineering that can introduce new properties or responsiveness to the system. Therefore, the application domains involving customization are limited because of the nature of the raw materials. By contrast, microbes are composed of a portfolio of single-celled living organisms that can be easily genetically modified to acquire new functions and are amenable to production in large-scale bioreactors, but have not yet been fully exploited to create environment-responsive materials.

Here, we propose to use genetically tractable microbial cells to create multifunctional, moisture-responsive interfaces. Generally, bio-derived materials, including nucleic acids (*13*), proteins (*14*), and polysaccharides (*15*), can change their structures or volumes when surrounding water activity is altered. Because these three materials are the basic biological components that form cellular structure, we hypothesized that microbial cells can be used as functional building blocks for constructing moisture-responsive materials. We speculated that a bilayer-structured biohybrid film could change shape and functions (fluorescence as an example) simultaneously with humidity change (Fig. 1). The concept of dual responsiveness is illustrated at the macroscopic level (Fig. 1, A and B), microscopic level (Fig. 1, C and D), cellular level (Fig. 1, E and F), and molecular level (Fig. 1, G and H). If this hypothesis were true, we could easily embed other functionalities into the existing moisture-responsive cells through modern genetic engineering technologies, such as clustered regularly interspaced short palindromic repeats (CRISPR)–Cas9 (*16*), for instance, to facilely introduce fluorophores (*17*), colors (*18*), odors (*19*), or other metabolic responsiveness induced by environmental change (*20*). This will open up a new application space for using hygroscopic transforming materials to tackle real-world problems related to moisture (for example, indoor humidity control and warts caused by hyperhidrosis). One intriguing application domain is designing wearable devices (*21*) to accommodate body sweat (*22*) for high-intensity working professionals including athletes and soldiers, to prevent frostbite or hypothermia. This research domain for regulating body condition has not been intensively pursued previously because of the lack of multifunctional hygroscopic materials that are facilely accessible, easy to process, and low-cost.

RESULTS

To prove that microbial cells can be used to create a hygroscopic structure that exhibits reversible shape transformation, we used the most common type of *Escherichia coli* cells to fabricate the biohybrid film. First, the cells were cultured and harvested to prepare a concentrated suspension for printing, before which all the nutrients (for example, sugar) were removed. Uncoated natural latex sheets (*cis*-1,4-polyisoprene, 150 to 500 μm thick) with rough surfaces (fig. S1) were selected as the moisture-inert materials, which demonstrated good bacterial biofilm

[1]Department of Chemical Engineering, Massachusetts Institute of Technology, Cambridge, MA 02139, USA. [2]MIT Media Lab, Massachusetts Institute of Technology, Cambridge, MA 02139, USA. [3]Department of Architecture, Massachusetts Institute of Technology, Cambridge, MA 02139, USA. [4]Department of Mechanical Engineering, Massachusetts Institute of Technology, Cambridge, MA 02139, USA. [5]Department of Biological Engineering, Massachusetts Institute of Technology, Cambridge, MA 02139, USA. [6]Department of Chemical and Biomolecular Engineering, National University of Singapore, Singapore 117585, Singapore. [7]New Balance Athletics, 190 Merrimack Street, Lawrence, MA 01843, USA.
*Corresponding author. Email: zhaox@mit.edu (X.Z.); dicwang@mit.edu (D.I.C.W.); ishii@media.mit.edu (H.I.)

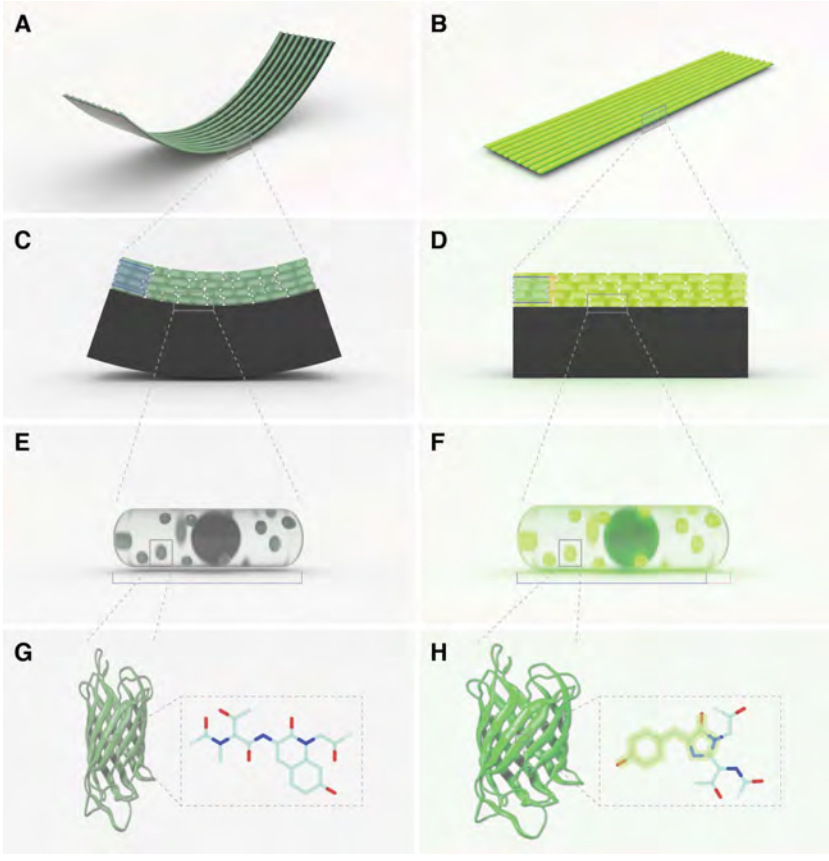

Fig. 1. An illustration showing the reversible transformation induced by the moisture gradient at different scales for a bilayer biohybrid film. (**A** and **B**) The film bends tangibly at low humidity levels (A) and becomes flat and glows at high humidity levels (B). (**C** and **D**) A cross section of the biohybrid film at the microscopic level, where dehydration of the cell layer (dark green and light green) coated on top of an inert thin film (black) enables the bending of the film at low humidity levels (C), whereas the film becomes flat at high humidity levels (D) through rehydration. The box on the top left corner indicates the contraction (C) and expansion (D) of cells under two conditions. (**E** and **F**) The change of cell size and cellular fluorescence with humidity levels due to moisture desorption (E) and adsorption (F) at the cellular level. (**G** and **H**) An example of the conformational change of intracellular eGFP at the molecular level due to water removal (G) and water binding (H) at different humidity levels.

adhesion through hydrophobic interactions (*23*) in the absence of additional chemical modification. By microprinting these cells (thickness, 1 to 5 μm) in parallel lines on the latex surface (fig. S2), a multifunctional biohybrid film was produced. When the film was introduced into dry conditions [relative humidity (RH), 15%], it immediately started to bend because of the contractile forces generated by cell dehydration (Fig. 2A), whereas the film flattened (Fig. 2B) with increasing environmental humidity (RH, 95%) by regaining water. This bending behavior (movie S1) was reversible over several cycles showing no hysteresis or distortion (Fig. 2C), as characterized in a customized humidity-controlled chamber (fig. S3). Using atomic force microscopy (AFM) imaging with humidity control (fig. S4), we observed similar phenomena at the cellular level, where single cells swelled or shrank along all three axes in response to changes in humidity (Fig. 2, D to F). This indicated that the bending effect of the tangible film was induced by the net force generated through the volume change of each individual cell (movie S2).

Beyond mechanical response to moisture, we sought to introduce additional functionalities through genetic engineering of the *E. coli* cells. Here, we used enhanced green fluorescent protein (eGFP) to demonstrate this concept. It is known that GFP will lose all of its fluoresce ability in ethanol because of dehydration (Fig. 1, G and H) (*24*). In our experiment, we found that the fluorescence intensity of biohybrid films using GFP-expressing *E. coli* (fig. S5 and table S1) was correlated with humidity (Fig. 2, G to I). The fluorescence intensity of the cell significantly decreased under dry conditions, consistent with dehydration-induced conformational changes of eGFP at low levels of water activity (*25*). When environmental humidity increased, eGFP renatured and the film re-exhibited fluorescence (movie S3). We further validated that eGFP itself changed fluorescence intensity under different conditions by imaging the cell lysate through confocal microscopy (fig. S6).

These sets of experiments verified our hypothesis that *E. coli* cells are naturally hydroscopic, which can process environmental information through shape transformation, whereas the multifunctionality can be easily introduced by genetic engineering. To generalize this concept to other types of microbial cells to suit the needs of different application domains, we measured the bending angles of a biohybrid film consisting of two Gram-positive bacteria (*Bacillus subtilis* and *Rhodococcus erythropolis*), two Gram-negative bacteria (*E. coli* and *Pseudomonas nitroreducens*), and baker's yeast (*Saccharomyces cerevisiae*), respectively (Fig. 2J). The results showed that different types of cells have similar moisture responsiveness, which indicates that this property may arise from macromolecular building blocks (nucleic acids, proteins, carbohydrates, and lipids) that are common to the cells. To examine this hypothesis, we investigated the bending behavior of the biohybrid films prepared by printing each of the four major intracellular macromolecules on latex (Fig. 2K). The results showed that with the same dry weight, proteins

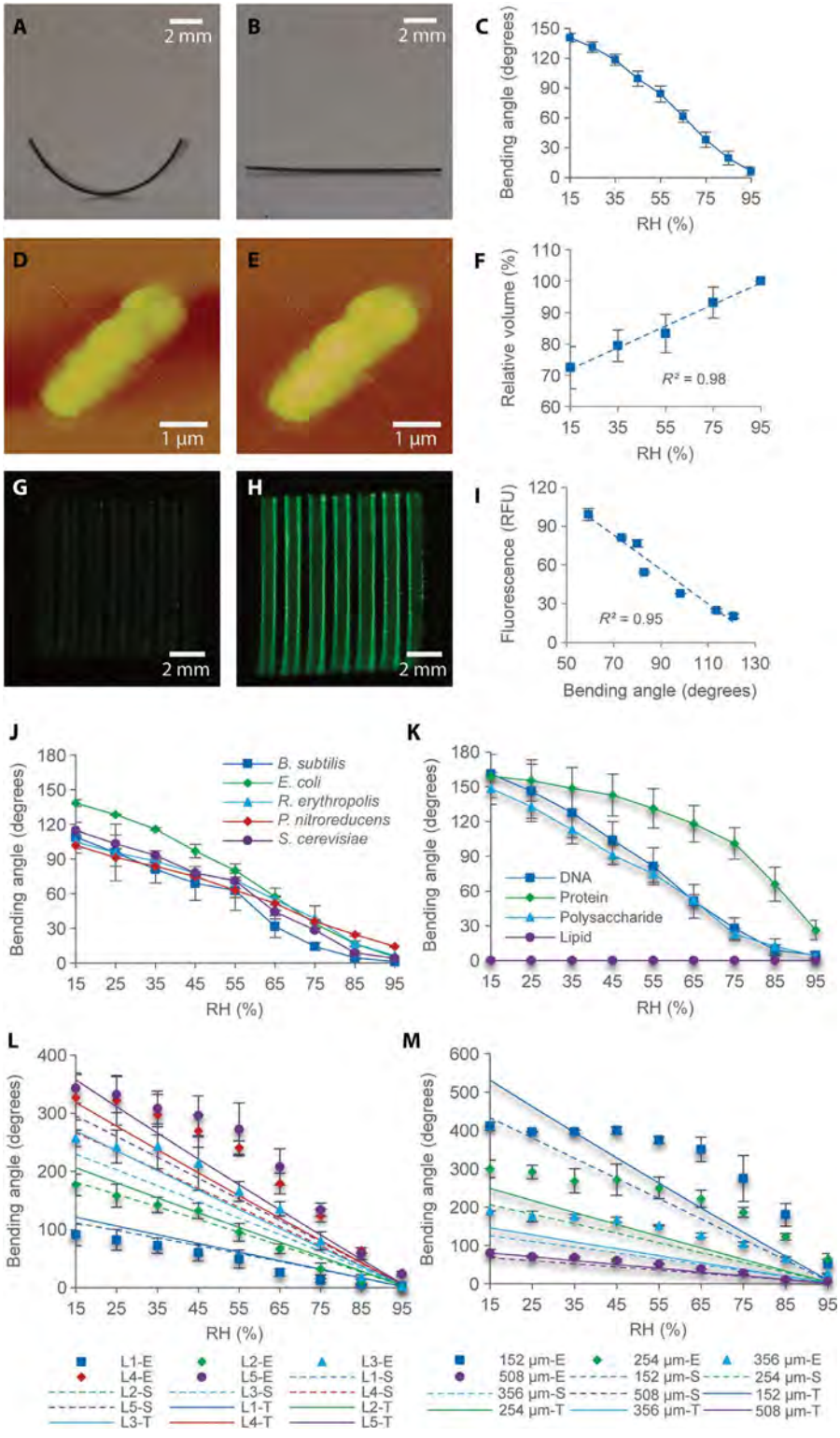

Fig. 2. Characterization of bilayer biohybrid films at different RH levels. (**A** and **B**) Shape transformation of a biohybrid film (1.2 cm × 0.9 cm) with a bilayer structure. The top layer is composed of *E. coli* cells (1 μm thick), and the bottom layer is a latex sheet (200 μm thick). It bends at 15% RH (A) and becomes flat at 95% RH (B). (**C**) The bending curvature of this biohybrid film at different RH levels. (**D** and **E**) Topological images of a cell at 15% RH (C) and 95% RH (D) obtained from AFM. (**F**) The cell volume change at different RH levels scanned by AFM. (**G** and **H**) Fluorescence images of a biohybrid film coated with *E. coli* with eGFP expression. It shows little fluorescence at 15% RH (G) compared with that at 95% RH (H). (**I**) Fluorescence intensity varies along with the bending curvature of the film when exposed to humid air in a dry environment. RFU, relative fluorescence units. (**J**) Bending angle for different types of cells. (**K**) Bending angle for major cellular biological components. (**L** and **M**) Simulation (symbol S) and theoretical model (symbol T) are consistent with experimentally measured bending (symbol E) for varying numbers of cell layer (symbol L) thickness (L) or latex substrate thickness (M).

induced a higher contractile force than nucleic acids and polysaccharides. As expected, lipids did not change the bending angles because the hydrophobicity of lipids prevented water absorption. This provides us with a pragmatic approach to further improve the bending performance by overexpressing proteins intracellularly using genetic engineering. The enlarged pool of hygroscopic biological materials including generally regarded as safe (GRAS) materials will definitely facilitate material selection in application and function customization. For instance, *S. cerevisiae* can be found on the surface of many fruits, and *B. subtilis* exists in soils—both sources are something humans are routinely in contact with—whereas nonpathogenic *E. coli* is a major member of natural human gut microbiota.

To quantitatively understand the mechanical performance of these hygroscopic materials, we measured the bending angles of the bilayer-structured biohybrid films (geometry in note S1) with varied cell layer and substrate thicknesses under different humidity conditions. The experimental data of the bending angle were then compared with a theoretical formula (Eq. 1) based on the classical Stoney formula (*26*) and the results from a three-dimensional finite-element model (fig. S7). The theoretical formula relates the bending angle, θ, to the contraction strain of the cell layer due to drying (decrease of the RH to a certain value at zero stress), ε_c^{dry}, and can be expressed as (note S2)

$$\theta = 360\frac{L}{2\pi R} = -180\frac{L}{\pi t_s}\frac{\alpha(1+\nu_c)(1+\varepsilon_c^{dry})\varepsilon_c^{dry}}{\frac{\bar{E}_s t_s}{6\bar{E}_c t_c} + \alpha\frac{2}{3}\left(1+\varepsilon_c^{dry}\right)} \quad (1)$$

where L is the length of the strip; R is the bending radius; t_s is the thickness of the latex substrate; t_c is the thickness of the microbial cell layer under zero stress; α is the fraction of surface area printed with the cells; E_s, ν_s and E_c, ν_c respectively denote Young's modulus and Poisson's ratio of the substrate and the cell layer; ε_c^{dry} is the contraction strain due to the drying (decrease of the RH) of the cell layer; and $\bar{E}_{s/v} = E_{s/v}/(1-\nu_{s/v}^2)$. AFM revealed that the volume depends linearly on humidity at the single-cell level (Fig. 2F), which can be described by the empirical relation in terms of the normalized volume $\bar{V}_c^{dry} = V_c^{dry}/V_c^{wet} = 0.345 \times \mathrm{RH} + 0.667$. The volume of the fully wet state is based on the measurement at 95% RH, the maximum value possible while avoiding the formation of water droplets.

The total volume change for the cell layer should also follow this relation, because the cells are densely packed to form a continuous film. Although the single cell exhibits anisotropic contraction, the average effect over a large amount of cells results in the cell layer deforming isotopically in each dimension. The contraction strain of the cell layer can thus be expressed as $\varepsilon_c^{dry} = \sqrt[3]{\bar{V}_c^{dry}} - 1$. Assuming that the thickness of each cell layer is 1 μm, $\nu_c = 0.3$, and using a constant value of the cell layer modulus as a fitting parameter, the proposed formula is in agreement (Fig. 2, L and M) with the experimentally measured bending angle for biohybrid films with different cell layer numbers and substrate thicknesses, except for the thinnest latex layers where large strains in the cell layer may lead to rearrangements or loss of contact between cells. The fitted elastic modulus of the cell layer is 70 MPa, consistent with previous reports (*27*); the stress and strain of the cell layer in the experiments were also estimated (fig. S8). Furthermore, the bending of the biohybrid films is well described by numerical simulation (movie S4 and note S3).

After characterizing the system, we turn to application of the biohybrid films for making wearables that respond to body sweat during motion. Because the bilayer structure curls naturally under ambient conditions (30 to 70% RH), which makes it hard to handle (for example, cutting, shaping, and assembling), we developed a sandwich structure where cell layers are coated on both sides of a moisture-inert material (Fig. 3A). This structure allows the film to respond only to a localized moisture gradient across the film (Fig. 3B) while ensuring the flatness of the film with balanced contractile forces on both sides (movie S5) in homogeneous environments (two sides exposed to the same condition). This biohybrid film with the sandwich structure is a robust fabric that responds to body sweat, where the bending degree can be adjusted and simulated by changing the thickness and elasticity of the middle supporting layer. By applying this responsive fabric that can reversibly change shape with the response to sweat production during exercise (Fig. 3C), we designed sports apparels with ventilating bio-flaps that can automatically adjust the moisture transfer and the heat resistance of the fabric through change of skin exposure percentage by modulating the area of exposed skin via shape transformation. Mechanical simulation was used to facilitate the design of the ideal shape deformation. In high heat–producing regions on the body, ventilating flaps with large unit size were used to enhance the air convection for fast moisture removal, whereas in high-sweat regions, high opening percentage was applied to ensure the permeability of the fabric (Fig. 3D) (*28*). This design, combined with the dynamic response of the fabric to moisture gradients, could smartly reflect and respond to the body's condition to enhance body core temperature control. With this technology, two wearables—a running suit and a shoe—were designed. First, the suit focusing on back ventilation (fig. S9) was designed on the basis of both a sweat map (*29*) and a heat map (*30*) (fig. S10) following the above-mentioned principles (Fig. 3E). The flaps opened up after 5 min of exercising (movie S6) when the test participants started to feel humid (Fig. 3, F and G). In the meantime, the temperature and humidity profile on the body was tracked using iButton sensors when wearing the garment in a temperature- and humidity-stable environment (Fig. 3, H and I). It showed that the suit with functional flaps could effectively remove sweat from the body and lower the temperature of the still air between the body and the fabric, compared with nonfunctional flaps with the same geometry (control). Following the first fabrication example, we designed a running shoe with multifunctional fluorescent flaps on the sole (fig. S11). It exhibited both shape and fluorescence intensity change under different humidity conditions (Fig. 3, J to O), where uncomfortable feeling and hygiene risk due to accumulation of feet sweat (for example, warts) can be innovatively avoided.

DISCUSSION

We harnessed the hygroscopic behavior of microbial cells, which provides us with a new perspective in using living materials for making moisture-responsive wearables that are multifunctional, interactive, and programmable. By characterizing and simulating the shape change effects in both homogeneous and heterogeneous environments, we designed two functional biohybrid prototypes that contain self-reproductive and genetically tractable cellular materials. These unique traits support the feasibility of scalable production of these functional materials for diverse applications.

Safety was our priority when we designed the prototypes. The garment used *B. subtilis*, which has the status of GRAS given by the U.S. Food and Drug Administration. Active *B. subtilis* can even be found in food products, such as Japanese natto soybean food, which has been shown to provide various health benefits to consumers (*31*). Hence,

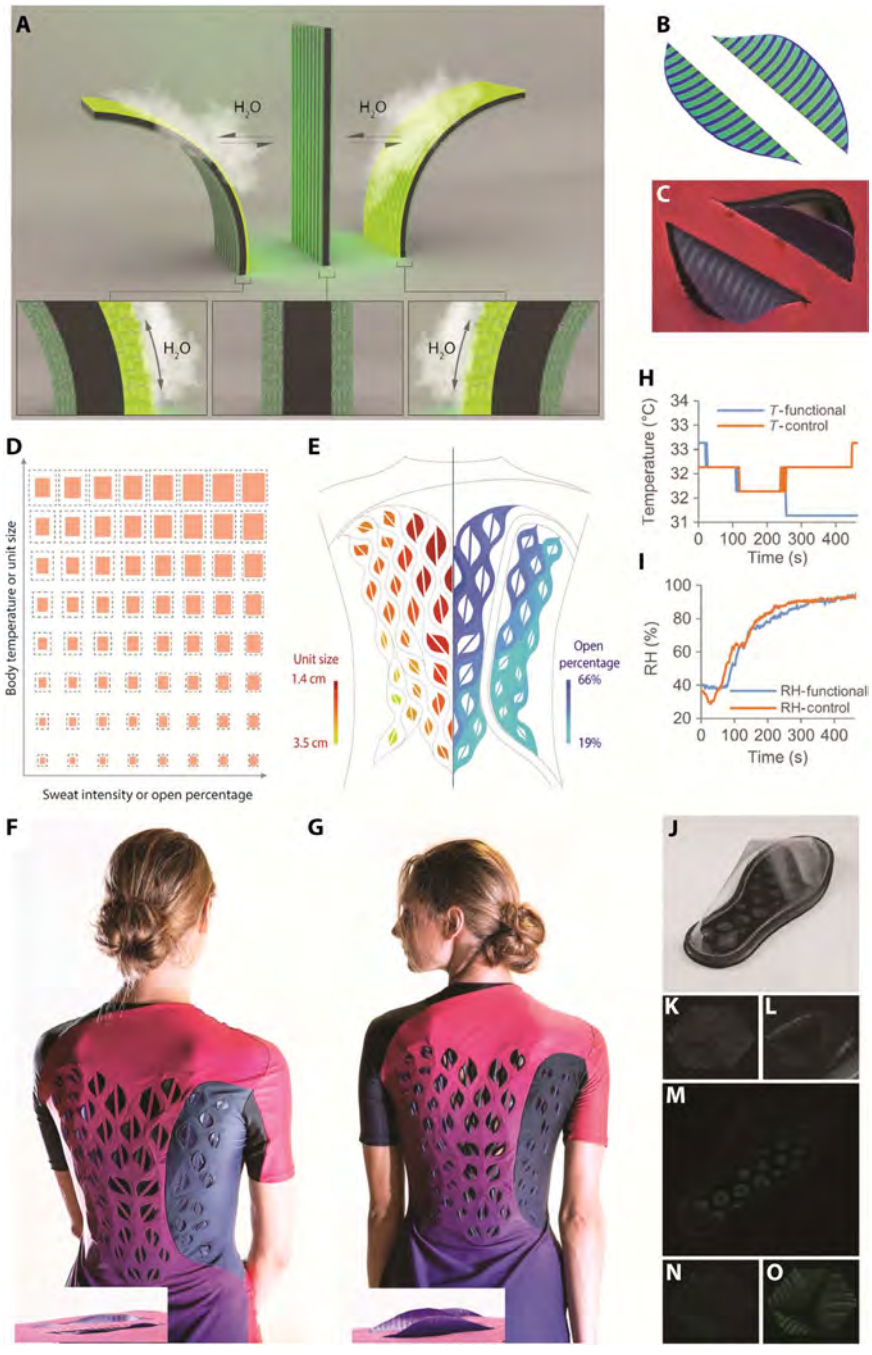

Fig. 3. Performance of sandwich-structured biohybrid film for making sweat-responsive wearables. (**A**) Shape transformation of a flat sandwich-structured biohybrid film when exposed to moisture. (**B** and **C**) Stress simulation (B) and experimental bending behavior (C) of a ventilating flap at the open stage when exposed to skin with high humidity. (**D**) Garment design principle considering both the amount of sweat and body temperature gradient during exercise (note S4). (**E**) Design of a female garment prototype based on heat maps (left, unit size) and sweat maps (right, percentage of opened area) of the back (note S5). (**F** and **G**) Images of garment prototype before exercise with flat ventilation flaps (F) and after exercise with curved ventilation flaps (G). (**H** and **I**) Temperature (H) or RH (I) profiles of stagnant air layer near volunteer skin when she wears the female garment with either functional flaps (blue) or nonfunctional flaps (orange). (**J** to **L**) The image of the shoe under transmitted light (J) and the flap on the sole at low (K) or high humidity (L). (**M** to **O**) The image of the shoe under fluorescence light (M) and the flap on the sole at low (N) or high humidity (O).

we conclude that wearing the garment or being exposed to it should not incur any safety concern. In the second application, the shoes are covered by genetically modified *E. coli*, which does not have GRAS status, though it is a nonpathogenic strain and is commonly used in the laboratory. We used *E. coli* here for proof of the concept, because genetic modification of this species was easy. The use of *E. coli* is strictly limited to the prototype stage and will be replaced by genetically modified GRAS species or natural fluorescent microbes in the commercialization stage. An additional safeguard strategy to be explored in the future is to replace active cells with cellular components, such as proteins and

nucleic acids, which have also been shown in this study to have moisture-responsive properties.

Future works should focus on the stability of the wearables. Although we have shown that the use of fabrics with microbes through 100 dry-wet cycles did not affect the bending performance of the fabrics (fig. S12), we believe that washability and durability of the wearables in different environments can be further improved by using novel design and chemistry, for example, using fibers with embedded bacteria and/or immobilizing microbes onto surfaces through covalent bonds. Additionally, wearable function maintenance (for example, cleaning and storage) should also be innovatively designed.

We foresee that this scalable and adaptable technology can be used in industries beyond fabricating wearable devices, where moisture gradient is a key factor, such as hydration enhancement in skin care products, humidity control in a smart home, and moisture removal in biomedical textiles.

MATERIALS AND METHODS

Chemicals, materials, and cells

Luria-Bertani (LB) medium, yeast extract–peptone-dextrose (YPD) medium, and agar were purchased from Becton Dickinson. The latex sheets with different thicknesses were purchased from both McMaster-Carr and MJTrends. Muscovite mica and sample mounting disks were purchased from Electron Microscopy Sciences (71856-01) and Bruker (SD-101). Glass slides for confocal imaging were purchased from VFM (SAH-2260-03A). Fluorescence source (Sola) and excitation filters for the camera were purchased from NIGHTSEA. The sensors for measuring body humidity and temperature (iButton DS1923) were purchased from Maxim Integrated. "Milliskin Matte" spandex fabric and black patterned spacer fabric were purchased from Spandex World Inc. Tuftane thermoplastic polyurethane was purchased from Perfectex Plus LLC. All other chemicals and reagents were purchased from Sigma-Aldrich. All other tools and materials were purchased from McMaster-Carr. We used the *E. coli* strain "MG1655_ΔrecA_ΔendA_DE3," harboring the plasmid "pET11a-eGFP-lacZ," which was obtained by cloning eGFP (Sequence 1) and *E. coli* lacZ into the commercial plasmid "pET11a" as a fusion protein. The *B. subtilis* strain "(pLS19) (pLS20) wild-type isolate" was purchased from Bacillus Genetic Stock Center. Baker's yeast *S. cerevisiae* was isolated from Red Star. We used *R. erythropolis* [ATCC (American Type Culture Collection) 53968] and *P. nitroreducens* HBP1 [DSMZ (German Collection of Microorganisms and Cell Cultures) 8897].

Preparing printing sample

All Gram-positive bacteria (*B. subtilis* and *R. erythropolis*), Gram-negative bacteria (*E. coli* and *P. nitroreducens*), and baker's yeast (*S. cerevisiae*) were cultured in 250-ml shake flasks. The cells were inoculated from a glycerol stock stored at −80°C into 50 ml of culture medium (LB for bacteria and YPD for yeast) in an Erlenmeyer shake flask and kept at 30°C with a shaking speed of 200 rpm overnight. For *E. coli*, additional ampicillin (100 mg/liter) was added to the medium in prior, and 0.1 mM isopropyl-β-D-thiogalactopyranoside was used to induce the expression of eGFP for another 24 hours when the culture's optical density at 600 nm (OD_{600}) reached 1.5 to 2.0. The cells were then harvested through centrifugation at 3000*g* for 5 min. Phosphate-buffered saline (PBS) was used for cell washing to remove all the medium components. Cell suspension was kept at 4°C for short-term storage. Before printing, the cells were resuspended to deionized water to prepare a ready-to-print cell suspension at a certain OD_{600} (ranging from 21.2 to 106). For other biological samples, it was prepared by dissolving lyophilized powder with a certain weight into deionized water or organic solvents depending on the solubility of the substance.

Deposition of biological materials onto humidity-inert substrate through bioprinting

Samples (cell suspension or biological solutions) were deposited onto the latex sheet through a microextrusion system (*32*). The latex substrate was framed on a flat printing platform, where the gap between the printing tip and substrate was about 0.5 mm. Typically, the extrusion speed was set between 5 and 8 μl/min, whereas the printer head moving speed was set at 20 cm/min. The biological sample's concentration or suspension density was estimated on the basis of the printing thread width, printing time, and required thickness. For the sandwich-structured biofilm, after printing one side of the substrate after it dried, the frame was flipped and the other side was then printed. Samples for bending curvature testing were cut by a rectangular cutting die.

Theoretical calculation regarding cell coating layers

On the basis of the scanning electron microscopy (SEM) images, we assumed that each individual cell coated on top of the latex film has a rectangular projection, with dimensions of 1 μm (width) × 3 μm (length), such that the area covered by each cell (A_{cell}) is 3 μm^2. During 1-min printing time, the extrusion tip will move 20 cm [tip moving speed (v_{tip}) = 20 cm/min], whereas the volume of extruded solution is 5 μl [dispensing volumetric rate ($V_{dispensing}$) = 5 μl/min]. From literature, we found that at OD_{600} = 1.0, the colony-forming unit (CFU/ml, number of cells) is 1.625×10^8. In general, we printed three times in the same position to minimize the coffee stain effect. With the above setting, the width of the cell film (W_{film}) after three prints with a cell suspension OD_{600} at ~20 is 0.775 mm (measured data). Thus, to cover a single layer of cells on top of a certain printing length (L_{film}) when printing three times, the OD_{600} required can be calculated on the basis of the following equation

$$OD_{600} = \frac{v_{tip} \times W_{film}}{3 \times A_{cell} \times V_{dispensing} \times \frac{CFU}{ml} \text{ per } OD_{600}}$$

By substituting the parameters in the current setting, the OD_{600} of cell suspension required to print a single layer is 21.2. Similarly, for coating multiple cell layers (N) on the inert substrate, the concentration (OD_{600}) of the cell suspension can be calculated ($N \times 21.2$).

Measurement from AFM

Before AFM, 1 ml of cell suspension (OD_{600} = 5.0) in PBS was centrifuged at 3000*g* for 5 min. The supernatant was carefully removed, followed by adding 1 ml of water, and the precipitated cell was dispersed. This washing process was repeated three times. The obtained sample (2 μl) was dropped to a freshly cleaved mica substrate and incubated at room temperature. After 10 min, the sample on the substrate was washed by 50 μl of water, and this washing process was repeated two times. The sample was dried, followed by scanning on AFM (Veeco Multimode with NanoScope V) in tapping mode with an NSC15/AIBS cantilever (MikroMasch). The AFM measurements were performed in 15 to 95% RH, with 20% as a step with a customized humidifier system (similar to fig. S3 but with an outlet tubing pointed to the sample). The measurements were conducted three times with different cells. The sizes

(length, width, and height) of the cell in the different RHs were analyzed on NanoScope Analysis software.

Sample bending curvature measurement

Sample bending curvature was measured in a humidity-controlled chamber (fig. S4). Before sample placement, the film was exposed to a 100% RH environment and then placed under room conditions (RH, 50%). This procedure was repeated for at least three cycles. The film was further transferred to the humidity chamber, and the bending curvature was monitored from 15 to 95% RH, with 10% as a step. The humidity was controlled through an RH sensor, which is located on the sample measurement platform. It can automatically adjust the chamber humidity to a target value by dry air and 100% humid air. The image of the bended sample was captured by a Canon EOS 5D Mark III camera, and the curvature was analyzed by customized curvature-measuring software built on top of a Rhino and Grasshopper platform.

Scanning electron microscopy

The film was coated with a 5- to 10-nm gold nanoparticle using a Gatan High Resolution Ion Beam Coater, and it was then imaged by a Zeiss Merlin high-resolution scanning electron microscope to observe high-resolution images. Noncoated samples were imaged using an FEI/Philips XL30 FEG emission scanning electron microscope.

Dark-field microscopy

Images were collected by a Nikon TE2000 inverted microscope with a 40×/0.60 numerical aperture objective using transmitted light from a 100-W halogen light source. Imaging was performed with MetaMorph software (version 7.8.4) and a Hamamatsu Orca-ER camera. Stream acquisition was performed with an exposure time of 20 ms. The images were collected with the camera chip center quadrant.

Confocal measurement

E. coli cells containing eGFP were lysed using the freeze-thaw method. The cell suspension was frozen in a −20°C freezer, and then the material was thawed at room temperature for several cycles. Cell pellets were removed by centrifugation at 3000*g*, while the green supernatant (containing eGFP) was transferred to a glass slide for confocal imaging. The humidity of the sample was adjusted through dry air or humid air during confocal imaging by Olympus FV300 (100×). The images were processed using Olympus FluoView version 4.2.a viewer.

Fluorescence measurement

The sample coated with cells containing eGFP was measured with a fluorescence source using a Canon EOS 5D Mark III camera with a Tiffen 49-mm yellow 12 filter with an excitation filter. The fluorescence image was analyzed by ImageJ to obtain the relative fluorescence unit before and after the humid air was applied to the samples.

Sensor on body testing

The iButton sensors (which monitor humidity and temperature) were mounted on the supporting frame of the garment with the sensing side toward skin. The resolution of the temperature measurement was set at 0.5°C, whereas the resolution of humidity was set at 0.6% RH. The data recording speed was set at 30 data points per minute. Two garments were used for testing: one with functional ventilation bio-flaps (functional garment) and the other one with nonfunctional ventilation flaps (control garment). The weight and the geometrical configuration of the two garments were the same. The temperature and humidity profiles of the participants were tracked by iButtons while each garment was worn during exercise.

SUPPLEMENTARY MATERIALS

Supplementary material for this article is available at http://advances.sciencemag.org/cgi/content/full/3/5/e1601984/DC1

note S1. Experimental data processing.
note S2. Theoretical prediction.
note S3. Finite-element simulation.
note S4. Garment design principle.
note S5. Flap design based on heat map and sweat map.
fig. S1. Surface properties of natural latex sheets characterized by SEM.
fig. S2. Bioprinter working principle.
fig. S3. Customized humidity-controlled chamber.
fig. S4. Single cell at different RHs imaged by AFM.
fig. S5. Map of plasmid pET11a-eGFP-lacZ.
fig. S6. Confocal images of cell lysate containing eGFP.
fig. S7. Strain and stress of biohybrid film at different RHs.
fig. S8. Mechanical characterization of a bilayer hybrid film.
fig. S9. Assembly of a female running suit focused on the back ventilation through heat press.
fig. S10. Running suit pattern design–based heat and sweat maps.
fig. S11. Design of the running shoe with multifunctional fluorescent flaps.
fig. S12. Sample stability test under 100 dry-wet cycles.
table S1. Sequence of the synthetic gene used in this study.
movie S1. Biohybrid bilayer film at different RHs.
movie S2. Single-cell volume change when decreasing RH imaged by dark-field microscopy.
movie S3. Fluorescence change of biohybrid film at different RHs.
movie S4. Simulation of bilayer biofilm bending.
movie S5. Simulation of sandwich-structured biofilm bending.
movie S6. Flaps opening for garment during exercise.

REFERENCES AND NOTES

1. L. López-Maury, S. Marguerat, J. Bähler, Tuning gene expression to changing environments: From rapid responses to evolutionary adaptation. *Nat. Rev. Genet.* **9**, 583–593 (2008).
2. S.-Y. Tee, A. R. Bausch, P. A. Janmey, The mechanical cell. *Curr. Biol.* **19**, R745–R748 (2009).
3. D.-H. Kim, D. D. Sarbassov, S. M. Ali, J. E. King, R. R. Latek, H. Erdjument-Bromage, P. Tempst, D. M. Sabatini, mTOR interacts with raptor to form a nutrient-sensitive complex that signals to the cell growth machinery. *Cell* **110**, 163–175 (2002).
4. E. Tzima, M. Irani-Tehrani, W. B. Kiosses, E. Dejana, D. A. Schultz, B. Engelhardt, G. Cao, H. DeLisser, M. A. Schwartz, A mechanosensory complex that mediates the endothelial cell response to fluid shear stress. *Nature* **437**, 426–431 (2005).
5. J. Deng, K. H. Schoenbach, E. S. Buescher, P. S. Hair, P. M. Fox, S. J. Beebe, The effects of intense submicrosecond electrical pulses on cells. *Biophys. J.* **84**, 2709–2714 (2003).
6. C. Dawson, J. F. V. Vincent, A.-M. Rocca, How pine cones open. *Nature* **390**, 668 (1997).
7. R. Elbaum, L. Zaltzman, I. Burgert, P. Fratzl, The role of wheat awns in the seed dispersal unit. *Science* **316**, 884–886 (2007).
8. E. Reyssat, L. Mahadevan, Hygromorphs: From pine cones to biomimetic bilayers. *J. R. Soc. Interface* **6**, 951–957 (2009).
9. M. Ma, L. Guo, D. G. Anderson, R. Langer, Bio-inspired polymer composite actuator and generator driven by water gradients. *Science* **339**, 186–189 (2013).
10. A. S. Gladman, E. A. Matsumoto, R. G. Nuzzo, L. Mahadevan, J. A. Lewis, Biomimetic 4D printing. *Nat. Mater.* **15**, 413–418 (2016).
11. X. Chen, D. Goodnight, Z. Gao, A. H. Cavusoglu, N. Sabharwal, M. DeLay, A. Driks, O. Sahin, Scaling up nanoscale water-driven energy conversion into evaporation-driven engines and generators. *Nat. Commun.* **6**, 7346 (2015).
12. A. Menges, Material computation: Higher integration in morphogenetic design. *Archit. Des.* **82**, 14–21 (2012).
13. J. Mertens, C. Rogero, M. Calleja, D. Ramos, J. A. Martín-Gago, C. Briones, J. Tamayo, Label-free detection of DNA hybridization based on hydration-induced tension in nucleic acid films. *Nat. Nanotechnol.* **3**, 301–307 (2008).
14. T. M. Raschke, Water structure and interactions with protein surfaces. *Curr. Opin. Struct. Biol.* **16**, 152–159 (2006).
15. A. C. Newns, The sorption and desorption kinetics of water in a regenerated cellulose. *Trans. Faraday Soc.* **52**, 1533 (1956).
16. L. Cong, F. A. Ran, D. Cox, S. Lin, R. Barretto, N. Habib, P. D. Hsu, X. Wu, W. Jiang, L. A. Marraffini, F. Zhang, Multiplex genome engineering using CRISPR/Cas systems. *Science* **339**, 819–823 (2013).

17. N. C. Shaner, R. E. Campbell, P. A. Steinbach, B. N. G. Giepmans, A. E. Palmer, R. Y. Tsien, Improved monomeric red, orange and yellow fluorescent proteins derived from *Discosoma* sp. red fluorescent protein. *Nat. Biotechnol.* **22**, 1567–1572 (2004).
18. H. Alper, K. Miyaoku, G. Stephanopoulos, Construction of lycopene-overproducing *E. coli* strains by combining systematic and combinatorial gene knockout targets. *Nat. Biotechnol.* **23**, 612–616 (2005).
19. G. M. Rodriguez, Y. Tashiro, S. Atsumi, Expanding ester biosynthesis in *Escherichia coli*. *Nat. Chem. Biol.* **10**, 259–265 (2014).
20. S. Aracic, S. Manna, S. Petrovski, J. L. Wiltshire, G. Mann, A. E. Franks, Innovative biological approaches for monitoring and improving water quality. *Front. Microbiol.* **6**, 826 (2015).
21. D. Son, J. Lee, S. Qiao, R. Ghaffari, J. Kim, J. E. Lee, C. Song, S. J. Kim, D. Jun Lee, S. W. Jun, S. Yang, M. Park, J. Shin, K. Do, M. Lee, K. Kang, C. S. Hwang, N. Lu, T. Hyeon, D.-H. Kim, Multifunctional wearable devices for diagnosis and therapy of movement disorders. *Nat. Nanotechnol.* **9**, 397–404 (2014).
22. J. A. Yaggie, T. Niemi, M. J. Buono, Sweat gland activity following thermal and cholinergic training. *Biol. Sport* **22**, 3–11 (2005).
23. M. C. M. Van Loosdrecht, J. Lyklema, W. Norde, G. Schraa, A. Zehnder, Electrophoretic mobility and hydrophobicity as a measured to predict the initial steps of bacterial adhesion. *Appl. Environ. Microbiol.* **53**, 1898–1901 (1987).
24. W. W. Ward, Biochemical and physical properties of green fluorescent protein. *Methods Biochem. Anal.* **47**, 39 (2006).
25. D. P. Barondeau, C. D. Putnam, C. J. Kassmann, J. A. Tainer, E. D. Getzoff, Mechanism and energetics of green fluorescent protein chromophore synthesis revealed by trapped intermediate structures. *Proc. Natl. Acad. Sci. U.S.A.* **100**, 12111–12116 (2003).
26. G. G. Stoney, The tension of metallic films deposited by electrolysis. *Proc. R. Soc. A Math. Phys. Eng. Sci.* **82**, 172 (1909).
27. J. A. Lichter, M. T. Thompson, M. Delgadillo, T. Nishikawa, M. F. Rubner, K. J. Van Vliet, Substrata mechanical stiffness can regulate adhesion of viable bacteria. *Biomacromolecules* **9**, 1571–1578 (2008).
28. G. Havenith, R. Heus, W. A. Lotens, Clothing ventilation, vapour resistance and permeability index: Changes due to posture, movement and wind. *Ergonomics* **33**, 989–1005 (1990).
29. C. J. Smith, G. Havenith, Body mapping of sweating patterns in athletes: A sex comparison. *Med. Sci. Sports Exerc.* **44**, 2350–2361 (2012).
30. R. Clark, B. Mullan, L. Pugh, Skin temperature during running—A study using infra-red colour thermography. *J. Physiol.* **267**, 53–62 (1977).
31. Y. Ikeda, M. Iki, A. Morita, E. Kajita, S. Kagamimori, Y. Kagawa, H. Yoneshima, Intake of fermented soybeans, *natto*, is associated with reduced bone loss in postmenopausal women: Japanese Population-based Osteoporosis (JPOS) Study. *J. Nutr.* **136**, 1323–1328 (2006).
32. L. Yao, J. Ou, G. Wang, C.-Y. Cheng, W. Wang, H. Steiner, H. Ishii, bioPrint: A liquid deposition printing system for natural actuators. *3D Printing Additive Manuf.* **2**, 168–179 (2015).

Acknowledgments: We thank A. Thielsen, J.-F. Fullum, T. Tenbroek, and A. Gutmann for thoughtful discussions. We thank Y. Yang for performing confocal experiment, S. Lin for performing Young's modulus measurement, W. Salmon for performing dark-field microscope imaging, X. Ma for the cell culture, and D. Dasarathy for proofreading. **Funding:** This research was supported by MIT Media Lab and Singapore-MIT Alliance X.Z. acknowledges support from the Office of Naval Research (no. N00014-14-1-0528). **Author contributions:** W.W., L.Y., D.I.C.W., X.Z., and H.I. conceived the idea. W.W., L.Y., R.K., D.I.C.W., X.Z., and H.I. designed the experiments. W.W., L.Y., C.-Y.C., T.Z., H.A., L.W., G.W., and O.A. performed the experiments and/or analyzed the data. H.S., J.O., K.Z., C.W., K.P., and A.M.B. contributed materials and/or tools. W.W., L.Y. and C.-Y.C. prepared the figures and videos. W.W., L.Y., T.Z., H.A., L.W., H.S., K.Z., R.K., and X.Z. reviewed and edited the manuscript. W.W., K.Z., R.K., and X.Z. wrote the paper. **Competing interests:** There is a nonprovisional patent related to this work filed with the U.S. patent office (Assignors: L.Y., W.W., J.O., C.-Y.C., G.W., H.I., D.I.C.W., H.S., C. Della Silva; application no. 14/927,375; filing date, 30 October 2015). The other authors declare that they have no competing interests. **Data and materials availability:** All data needed to evaluate the conclusions in the paper are present in the paper and/or the Supplementary Materials. Additional data related to this paper may be requested from the authors.

Submitted 22 August 2016
Accepted 22 March 2017
Published 19 May 2017
10.1126/sciadv.1601984

Citation: W. Wang, L. Yao, C.-Y. Cheng, T. Zhang, H. Atsumi, L. Wang, G. Wang, O. Anilionyte, H. Steiner, J. Ou, K. Zhou, C. Wawrousek, K. Petrecca, A. M. Belcher, R. Karnik, X. Zhao, D. I. C. Wang, H. Ishii, Harnessing the hygroscopic and biofluorescent behaviors of genetically tractable microbial cells to design biohybrid wearables. *Sci. Adv.* **3**, e1601984 (2017).

ScienceAdvances
AAAS

Harnessing the hygroscopic and biofluorescent behaviors of genetically tractable microbial cells to design biohybrid wearables

Wen Wang, Lining Yao, Chin-Yi Cheng, Teng Zhang, Hiroshi Atsumi, Luda Wang, Guanyun Wang, Oksana Anilionyte, Helene Steiner, Jifei Ou, Kang Zhou, Chris Wawrousek, Katherine Petrecca, Angela M. Belcher, Rohit Karnik, Xuanhe Zhao, Daniel I. C. Wang and Hiroshi Ishii (May 19, 2017)
Sci Adv 2017, 3:.
doi: 10.1126/sciadv.1601984

Science Advances

AAAS

advances.sciencemag.org/cgi/content/full/3/5/e1601984/DC1

Supplementary Materials for

Harnessing the hygroscopic and biofluorescent behaviors of genetically tractable microbial cells to design biohybrid wearables

Wen Wang, Lining Yao, Chin-Yi Cheng, Teng Zhang, Hiroshi Atsumi, Luda Wang, Guanyun Wang, Oksana Anilionyte, Helene Steiner, Jifei Ou, Kang Zhou, Chris Wawrousek, Katherine Petrecca, Angela M. Belcher, Rohit Karnik, Xuanhe Zhao, Daniel I. C. Wang, Hiroshi Ishii

Published 19 May 2017, *Sci. Adv.* **3**, e1601984 (2017)
DOI: 10.1126/sciadv.1601984

The PDF file includes:

Other Supplementary Material for this manuscript includes the following:
(available at advances.sciencemag.org/cgi/content/full/3/5/e1601984/DC1)

- movie S1 (.avi format). Biohybrid bilayer film at different RHs.
- movie S2 (.avi format). Single-cell volume change when decreasing RH imaged by dark-field microscopy.
- movie S3 (.avi format). Fluorescence change of biohybrid film at different RHs.
- movie S4 (.avi format). Simulation of bilayer biofilm bending.
- movie S5 (.avi format). Simulation of sandwich-structured biofilm bending.
- movie S6 (.avi format). Flaps opening for garment during exercise.

note S1. Experimental data processing.

Radius of curvature can be calculated directly from the bending angle: $R = \frac{L}{2\pi\theta/360}$, where L is the length of the latex film. Strain of the compressed surface is given by

$$\varepsilon = \frac{2}{3} \cdot \frac{t_s}{R}$$

where t_s is the thickness of latex, and R is the curvature of the latex on stretched side.

Force per unit length (N/m) of the latex surface is given by Stoney formula under plan strain condition

$$F = \frac{1}{6} \frac{E_s}{1 - \upsilon_s^2} \cdot \frac{t_s^2}{R}$$

Where E and $\upsilon_s$are latex's Young's modulus (3 MPa) and Poisson's ratio (0.5), respectively, t_s is the thickness, and R is the curvature

Stress on the cell layer is

$$\sigma = \frac{F}{t_c} \cdot \frac{w_c + w_{gap}}{w_c}$$

where t_c is the thickness of the cell (5 μm), w_c and w_{gap} are the width of the cell strip and width of the gap area (fig. S8A), respectively.

note S2. Theoretical prediction.

The bending deformation of a bilayer biohybrid film is shown in fig. S8. As shown in fig. S8B, the cell layer has a thickness t_c, and the thickness of latex is denoted as t_s. The hybrid film will bend and reach an equilibrium radius R after the contracting (drying) (fig. S8C). According to the Stoney formula under plane strain condition, we have

$$\overline{E}_s \frac{t_s^2}{6R} = F$$

where $\overline{E}_s = \frac{E_s}{1-\nu_s^2}$, E_s and ν_s are the Young's modulus and Poisson's ratio of latex substrate, F represents the force per unit length generated by the cell layer.

The strain of the cell layer contains two contributors, the contractile strain (at zero stress) due to drying $\varepsilon_c^{dry} < 0$ and the tensile strain ε_c^{def} induced by the resistance of the latex layer due to bending. The total strain in the top cell layer is

$$\varepsilon_c = \varepsilon_c^{def} - \varepsilon_c^{dry} = -\frac{2t_s}{3R} - \varepsilon_c^{dry}$$

The cell layers are constrained by the substrate along x_2 direction, and this will also contribute to the cell stress through the Poisson effect and leads to the following formula for the stress inside the cell layer

$$\sigma_c = \overline{E}_c\left(\varepsilon_c - \nu_c\varepsilon_c^{dry}\right) = \overline{E}_c\left(-\frac{2t_s}{3R} - \left(1+\nu_c\right)\varepsilon_c^{dry}\right)$$

where $\overline{E}_c = \frac{E_c}{1-\nu_c^2}$. Note that σ_{33} inside the cell layer is assumed to be 0, as the cell layer can freely deform along x_3 direction and the thickness of the cell layer is very small.

The thickness of the cell layer also changes during the drying and can be expressed as

$$t_c^{dry} = t_c\left(1+\varepsilon_c^{dry}\right)$$

The thickness of cell layer will further change after taking the bending deformation of the cell layer into account, whose effect on the stress calculation is neglected in the framework of linear elasticity.

The total force in the cell layer is

$$F = \sigma_c t_c^{dry} = \overline{E}_c t_c\left(1+\varepsilon_c^{dry}\right)\left(-\frac{2t_s}{3R} - \left(1+\nu_c\right)\varepsilon_c^{dry}\right)$$

Comparing with the result based on the Stoney formula leads to

$$F = \overline{\overline{E}}_s \frac{t_s^2}{6R}$$
$$\Rightarrow \overline{\overline{E}}_s \frac{t_s^2}{6R} = \alpha \overline{\overline{E}}_c \left(1+\varepsilon_c^{dry}\right)\left(-\frac{2t_s}{3R} - \left(1+\nu_c\right)\varepsilon_c^{dry}\right)t_c$$

where α is the coverage of the cell to account for the gap between the cell lines. The final bending curvature for the single layer is

$$\kappa = \frac{1}{R} = -\frac{1}{t_s}\frac{\alpha\left(1+\nu_c\right)\left(1+\varepsilon_c^{dry}\right)\varepsilon_c^{dry}}{\frac{\overline{\overline{E}}_s t_s}{6\overline{\overline{E}}_c t_c} + \frac{2}{3}\alpha\left(1+\varepsilon_c^{dry}\right)}$$

For a given long strip (with length of *L*) of the bio-hybrid film, the bending angle can be expressed as

$$\theta = \kappa = 360\frac{L}{2\pi R} = -180\frac{L}{\pi t_s}\frac{\alpha\left(1+\nu_c\right)\left(1+\varepsilon_c^{dry}\right)\varepsilon_c^{dry}}{\frac{\overline{\overline{E}}_s t_s}{6\overline{\overline{E}}_c t_c} + \alpha\frac{2}{3}\left(1+\varepsilon_c^{dry}\right)} \qquad (*)$$

It should be noted that Eq. (*) is derived in the framework of linear elasticity and the fully nonlinear analysis will be performed with finite element simulation as described in next section. The coverage ratio according to the experiments is set to be $\alpha = \frac{8}{13}$. If $\frac{\overline{\overline{E}}_s t_s}{6\overline{\overline{E}}_c t_c} >> 1$, and the bending angle can be simplified as

$$\theta = -180\frac{L}{\pi t_s}\frac{6\alpha\overline{\overline{E}}_c t_c}{\overline{\overline{E}}_s t_s}\left(1+\nu_c\right)\left(1+\varepsilon_1^{dry}\right)\varepsilon_1^{dry}$$

The above equation indicates the linear relationship between the cell layer thickness and bending angle observed in the experiments.

Fitting the experimental data with Eq. 1 in the main text and assuming $\nu_c = 0.3$, we can obtain

$$\overline{\overline{E}}_c \approx 19\overline{\overline{E}}_s$$

Note that the Poisson ratio of the cell layer is an assumption.

note S3. Finite-element simulation.

We developed a three-dimensional finite-element model to simulate the bending deformation of the biohybrid films, including the bilayer structure and sandwich structure. The simulated bilayer structure is a rectangle long strip with length as 12.0 mm and width as 9.1 mm. We did two set of simulations to test the effect of changing cell layer thickness and substrate thickness. For the first set of simulations, the thickness of the cell layer changed from 1 to 5 μm and the substrate thickness was fixed as 0.2 mm. We also ran simulations with the cell layer thickness fixed at 5 μm and varied the substrate thickness from 0.15 to 0.51 mm. The elastic property of the cell layer was modeled as linear elastic materials with geometry nonlinear deformation. The Young's modulus and Poisson's ratio were taken as 70 MPa and 0.3 by fitting experimental data. The latex substrate is described as incompressible Neo-Hookean material with Young's modulus as 3 MPa.

All the numerical simulations were carried out with ABAQUS/Standard. The cell layer was modeled with the C3D8R element and the latex substrate was simulated with C3D8RH to describe the incompressibility of the rubber materials. The contracting and swelling behaviors of the cell layer are modeled as thermal contraction and expansion in the numerical simulations. Typical bending of the bio-hybrid films from simulations can be found in movie S4.

note S4. Garment design principle.

When designing the garment, the size of bio-hybrid flap was estimated based on the body temperature profile. At low body temperature regions, where skin is sensitive to heat loss, smaller size of flaps were applied to keep the still air layer adhesive to the body, so that heat loss induced by environmental air turbulence could be avoided. In Fig. 3D, the Y axis represents the body temperature, and the orange colored block area indicates the size of the flaps. It is clear that at low body temperatures, the area of the blocks are smaller than those at high body temperature.

Similarly, the percentage of skin exposure (or open percentage) is designed based on sweat intensity. The open percentage indicates the total ratio of the skin exposed in a certain defined area (it can contain one big flap or several small flaps, but with the same open percentage). In Fig. 3D, the x axis depicts that the sweat intensity changes. The dashed line indicates the defined area under consideration, while the block indicates the flap size. It can be seen that at a fixed sweat intensity, the area percentage of the orange

block inside the dashed line region is a fixed number. When increasing the sweat intensity, the open percentage increases.

note S5. Flap design based on heat map and sweat map.

The design of the bio-flap considered two important parameters: body temperature (represented by unit size) and sweat intensity (represented by open percentage). In fig. 3E, the left side of body shows how unit size is changing based on different body temperature at different locations (fig. S10, A and B), and each unit size is different (ranging from 1.4 cm to 3.5 cm) with consideration of heat removal efficiency and current fabrication limitations. The right side of the body represents the relationship between the open percentage and the sweat intensity (fig. S10, C and D). The boundaries between each defined area is highlighted, and the color intensity indicates the ratio of the open area is adjusted (19–66%) based on different sweat rate (170–800 g/m^2-h).

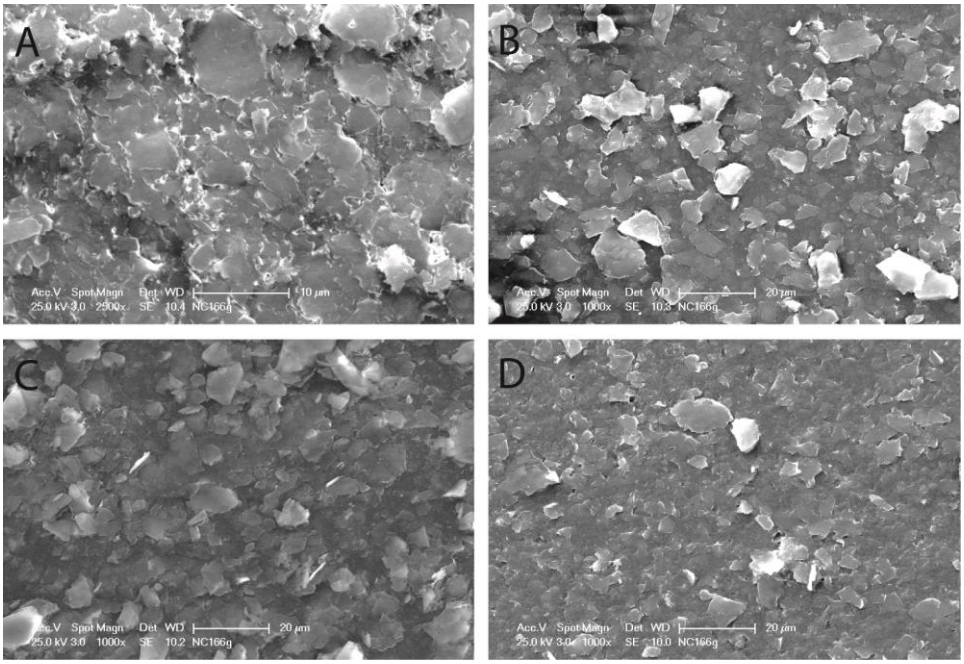

fig. S1. Surface properties of natural latex sheets characterized by SEM. Latex thickness: (**A**) 152 μm (**B**) 254 μm (**C**) 356 μm (**D**) 508 μm.

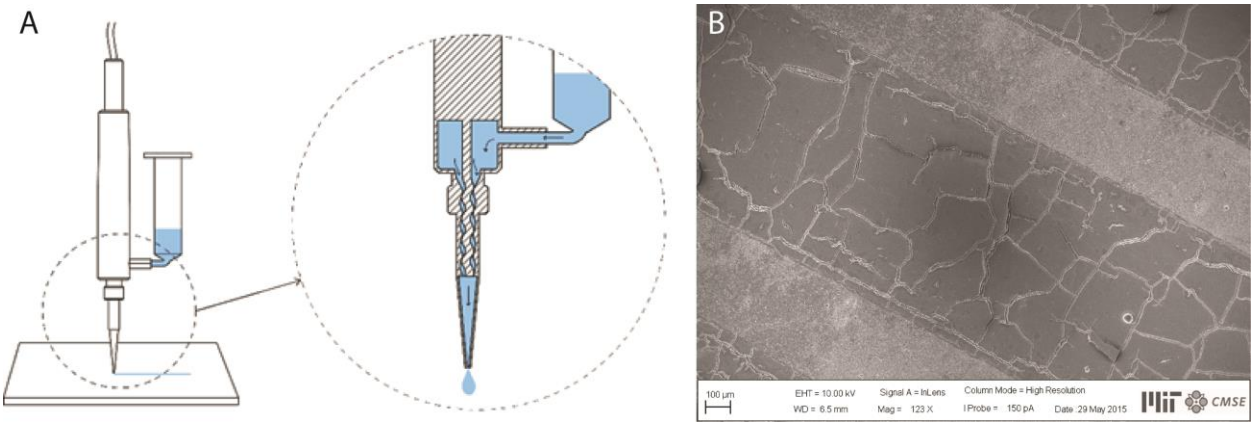

fig. S2. Bioprinter working principle. (**A**) Microdeposition bio-printer to deposit biological samples through extrusion. (**B**) SEM image of deposited cell thread (cracks were formed due to vacuum in SEM chamber).

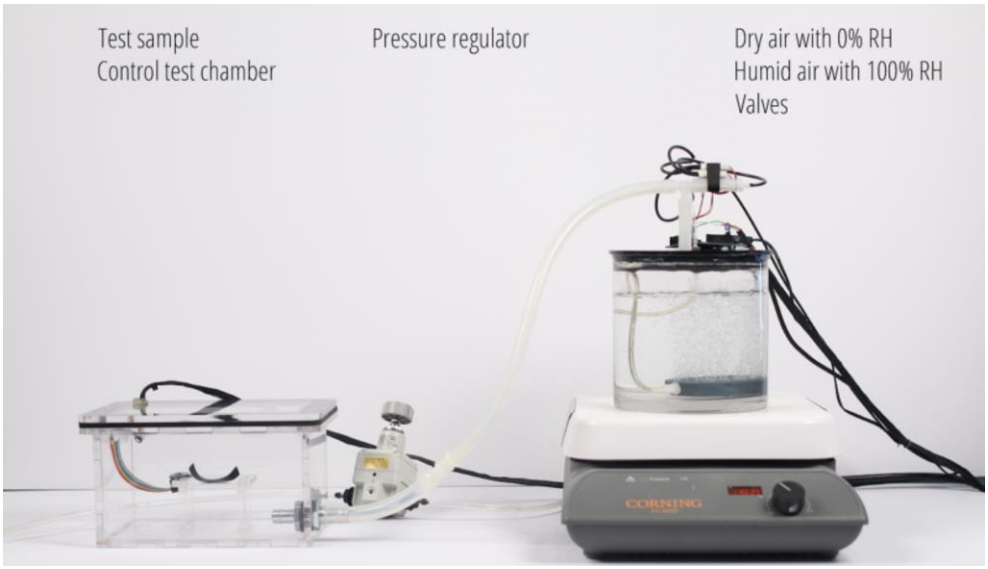

fig. S3. Customized humidity-controlled chamber. The setup include three main parts: The first module is the digital humidity sensor that is contained within the humidity control box. The second module is the controlled air source. There are two air streams that contain 0% RH and 100% RH respectively. The third module is the interface and control module. Through the computer interface, users can input desired RH for the test chambers. It takes between 20 seconds to 1 minute for the system to react and reach the desired RH. The equipped digital humidity sensor (HTU21D(F), Adafruit) has a

typical accuracy of ±2% with an operating range that is optimized from 5% to 95% RH, and is connected via I2C to the control interface.

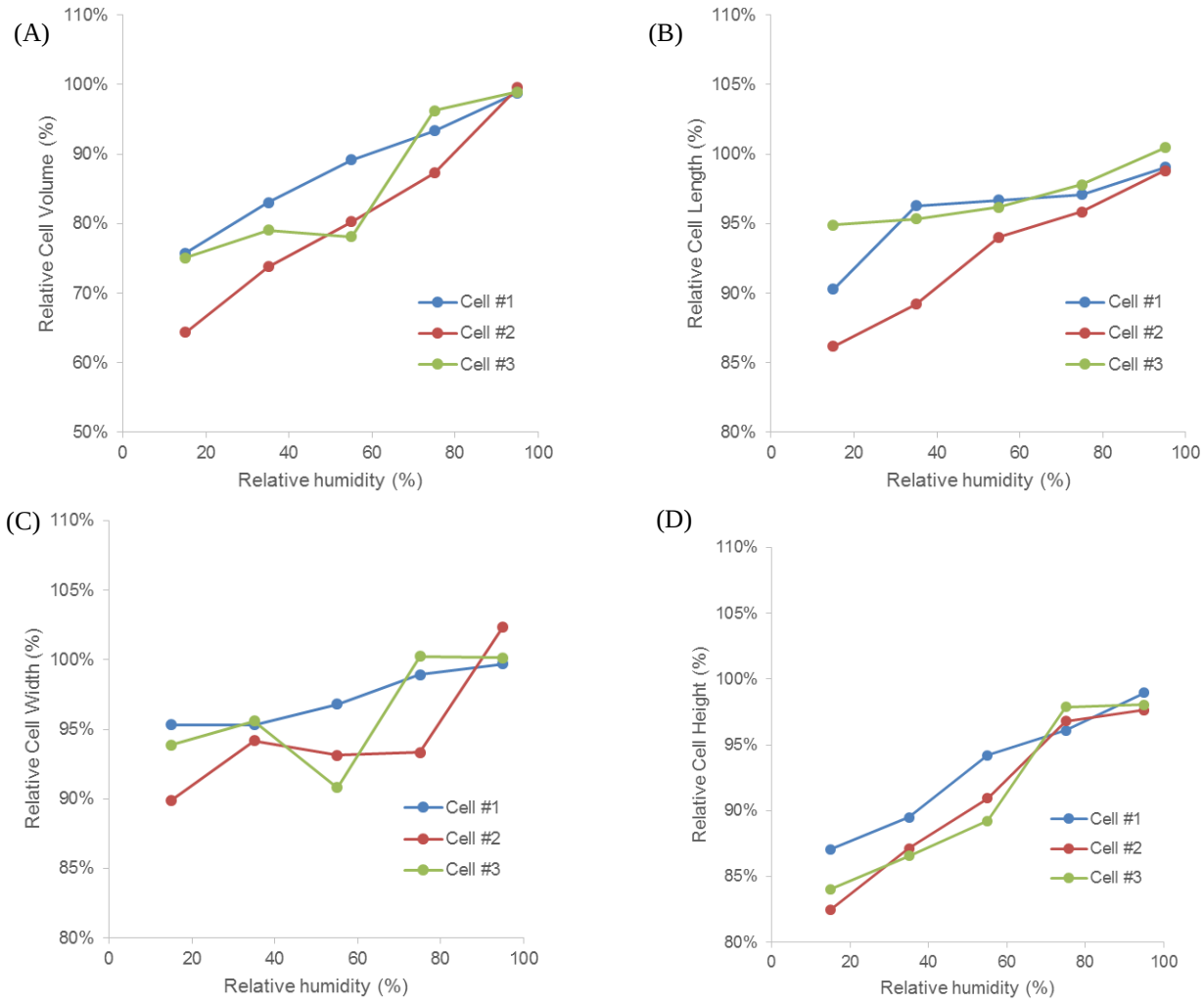

fig. S4. Single cell at different RHs imaged by AFM. (**A**) relative volume, (**B**) relative length, (**C**) relative width, and (**D**) relative height.

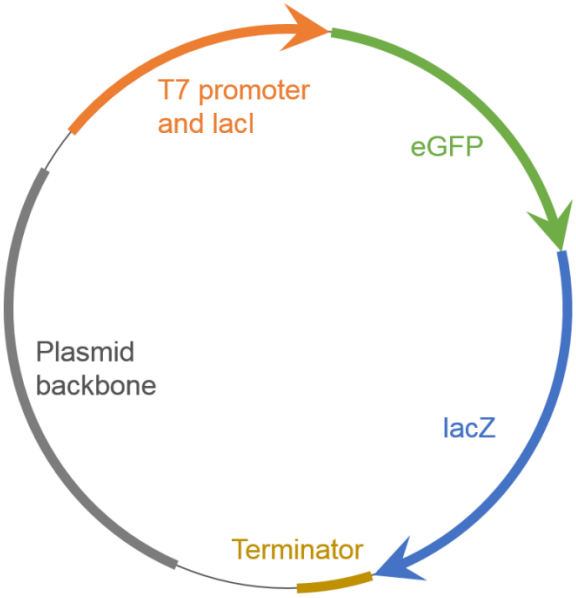

fig. S5. Map of plasmid pET11a-eGFP-lacZ.

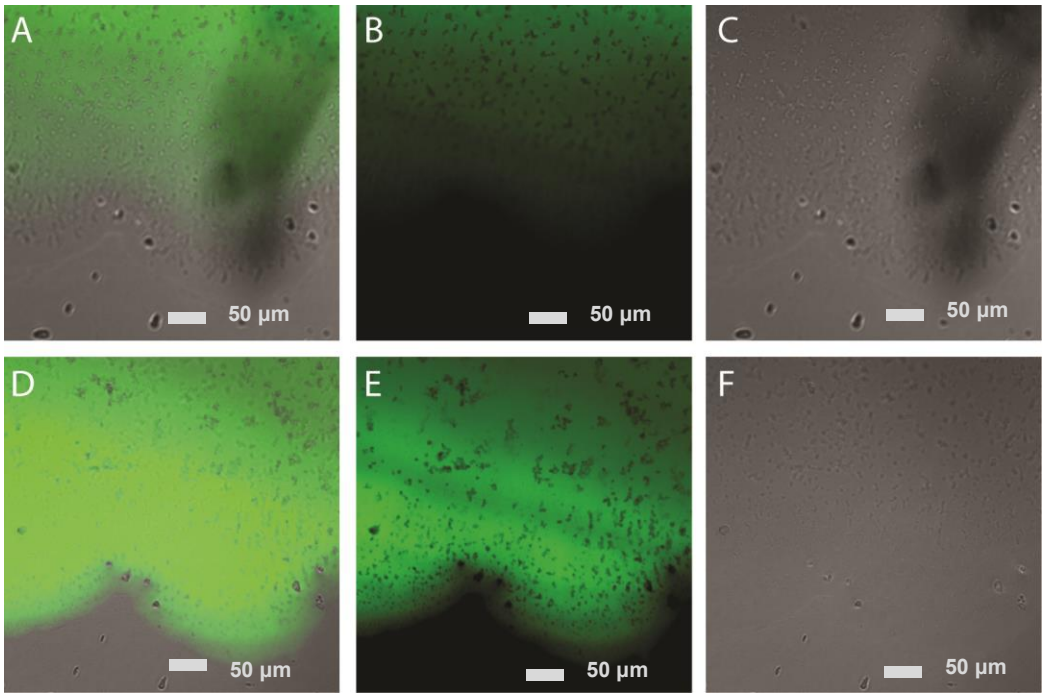

fig. S6. Confocal images of cell lysate containing eGFP. (**A**–**C**) Image of a dried sample with merged channels (A), fluorescence channel (B), and under transmitted light (C). (**D**–**F**) Image of humidified sample with merged channels (D), fluorescence channel (E), and under transmitted light (F). Some of the grey dots under transmitted light (C and F) might be cellular soluble materials. They might be partially dissolved (F) at high humidity condition, comparing imaging at low humidity (C) by changing the reflective index.

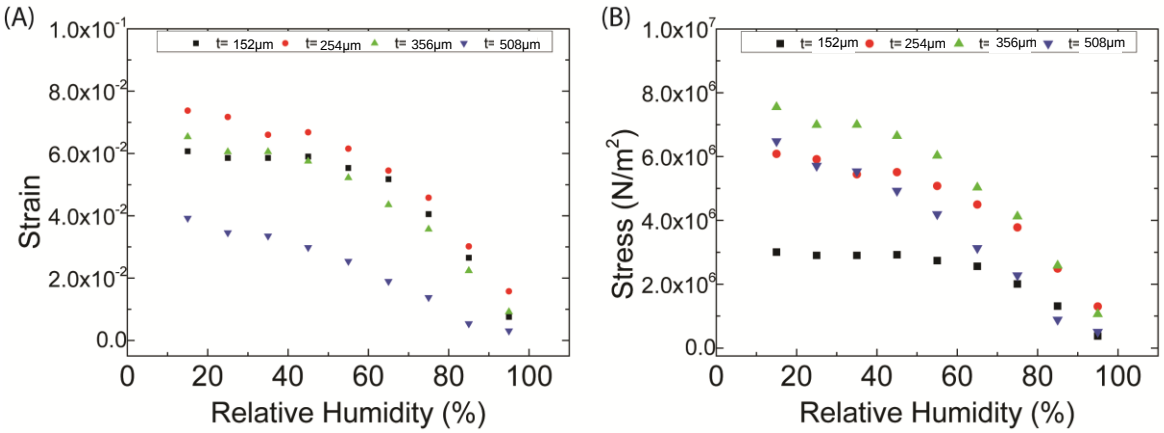

fig. S7. Strain and stress of biohybrid film at different RHs.

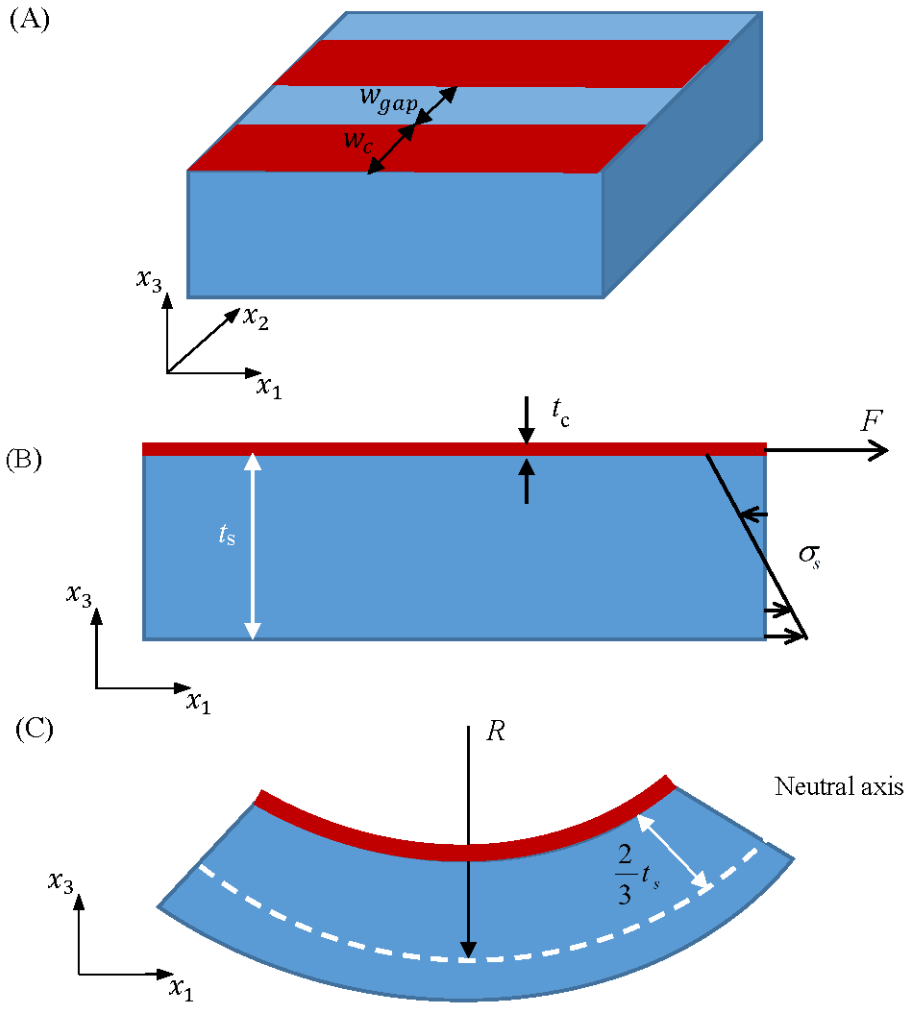

fig. S8. Mechanical characterization of a bilayer hybrid film. (**A**) Schematic of the structure of cell layer (red) and substrate (blue). (**B**) Bending deformation of a biohybrid film when swelling. (**C**) Bending deformation of a biohybrid film when contracting.

fig. S9. Assembly of a female running suit focused on the back ventilation through heat press. Layers from the top to the bottom (from the layer that is the closest to the skin) are mesh fabric for spacing, thermoplastic polyurethane (TPU) for bonding with applied heat, stretchy fabric, TPU for bonding, functional bio-flaps, TPU for bonding, and stretchy fabric as the main back panel.

(A)

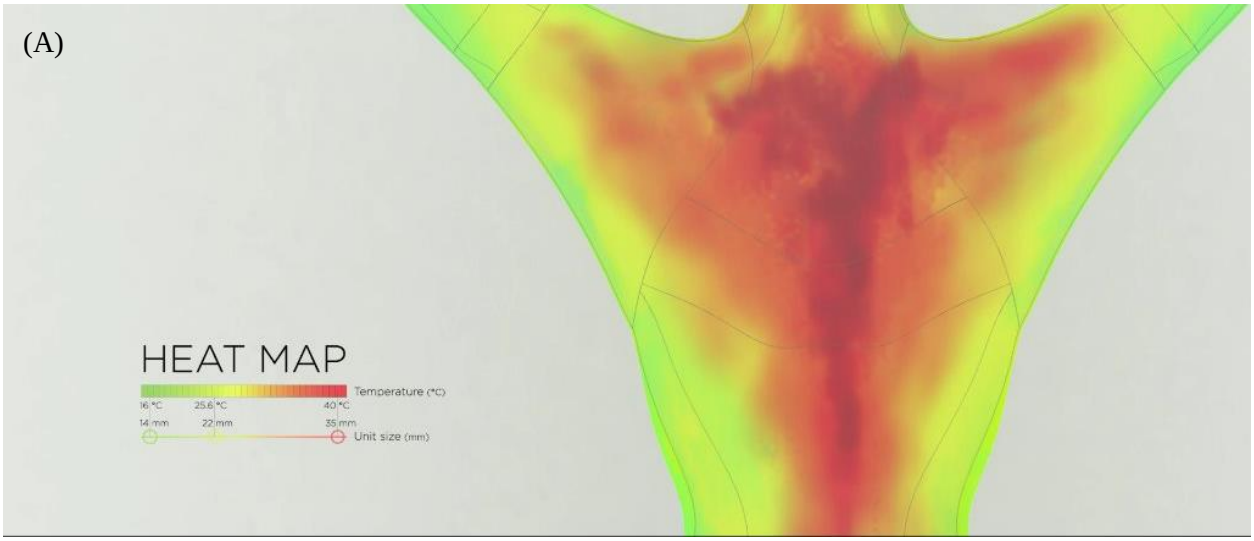
HEAT MAP
Temperature (°C)
16 °C
25.6 °C
40 °C
14 mm
22 mm
35 mm
Unit size (mm)

(B)

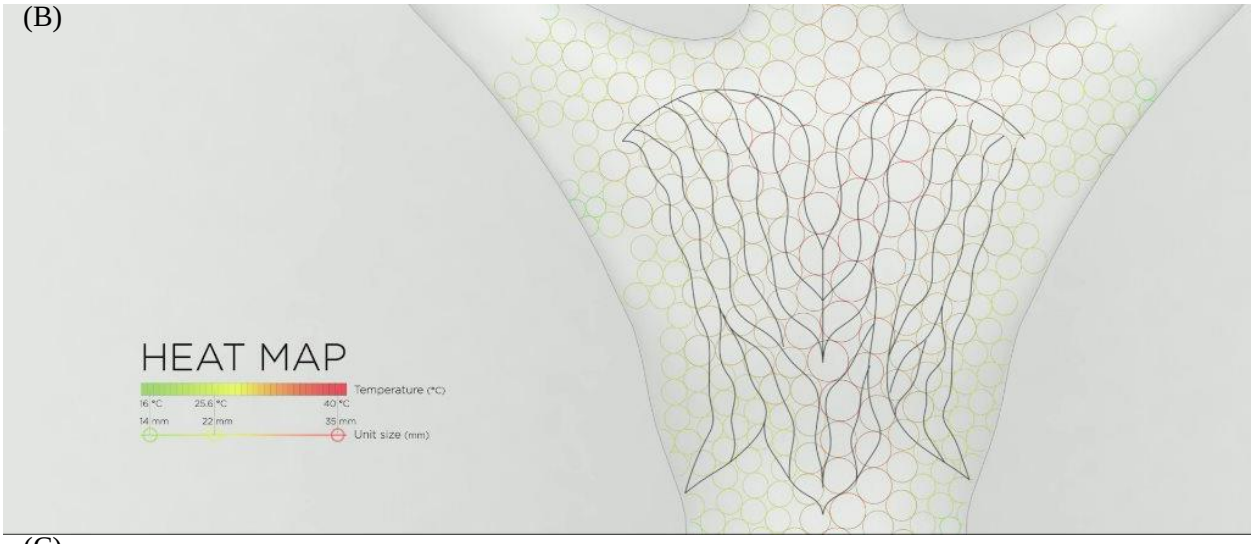
HEAT MAP
Temperature (°C)
16 °C
25.6 °C
40 °C
14 mm
22 mm
35 mm
Unit size (mm)

(C)


SWEAT MAP
Sweat amout (g/m2hr)
170 g/m²hr
495 g/m²hr
900 g/m²hr
19 %
34 %
66 %
Opening rate (%)

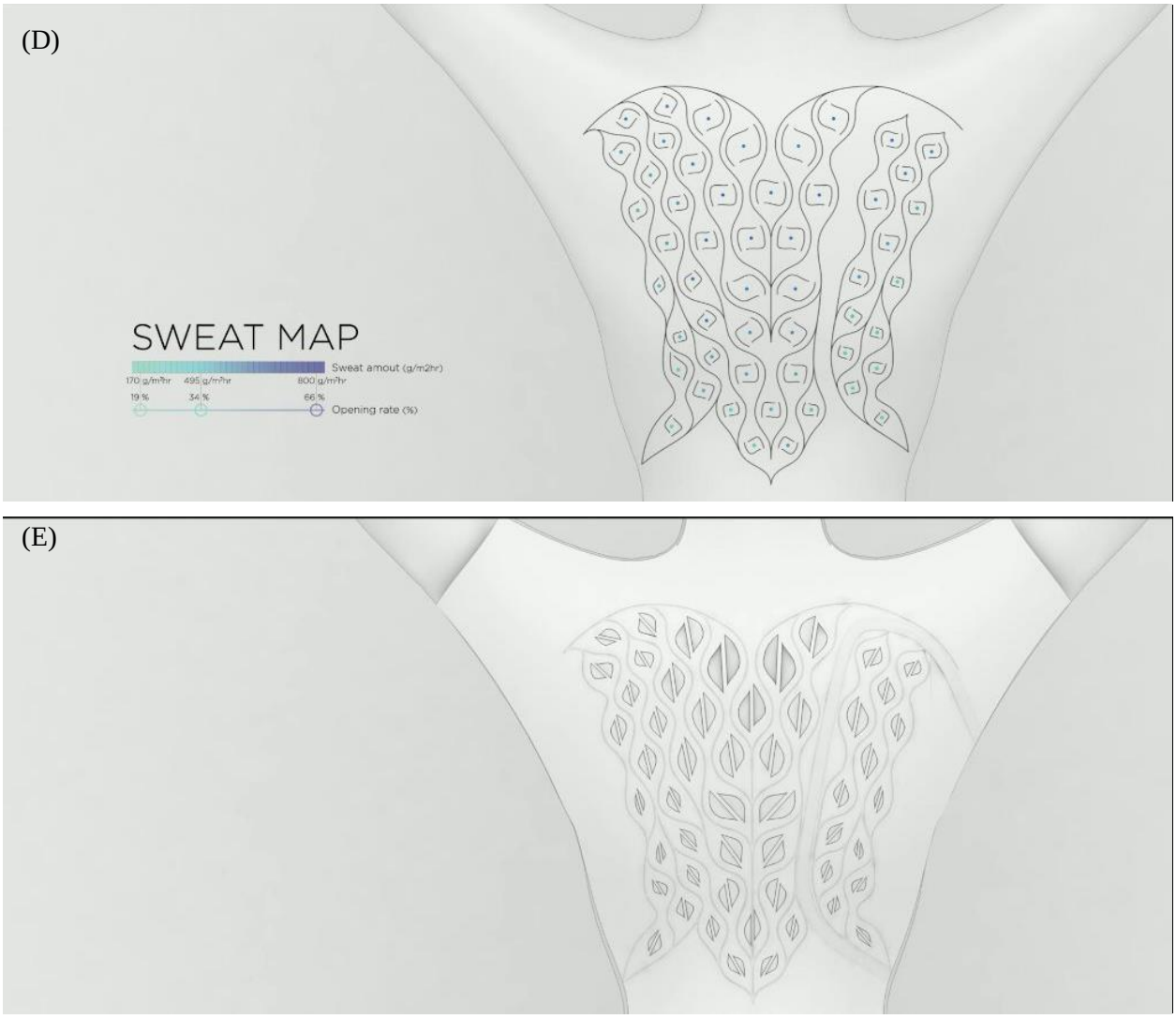

fig. S10. Running suit pattern design based heat and sweat maps. (**A**) Heat map (*30*) of the back. (**B**) Unit size pattern design based on heat profile simulation. (**C**) Sweat map (*29*) of the back. (**D**) Gap pattern design based on sweat intensity simulation. (**E**) Optimized flap pattern design considering esthetics.

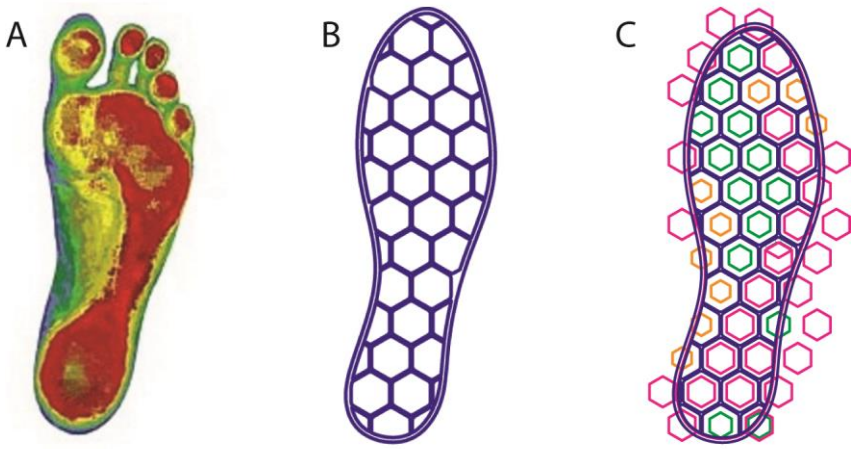

fig. S11. Design of the running shoe with multifunctional fluorescent flaps. (**A**) Heat map of a right foot. (**B**) Hexagon allocation on the shoe sole. (**C**) Flap design considering heat map.

(A)

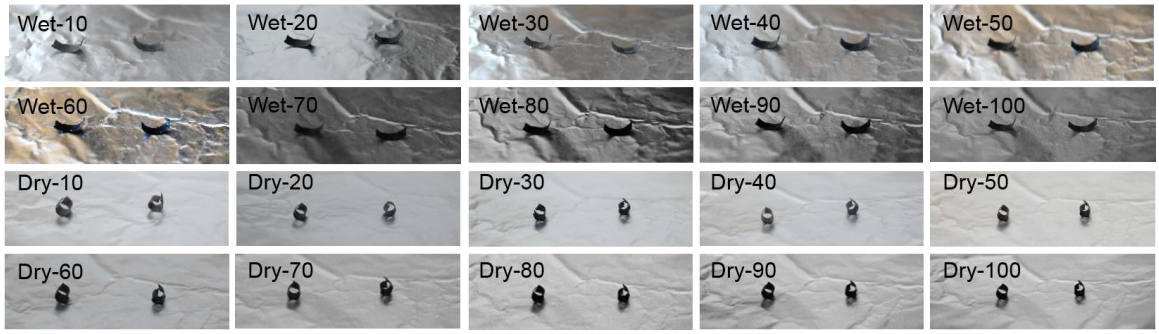

(B)

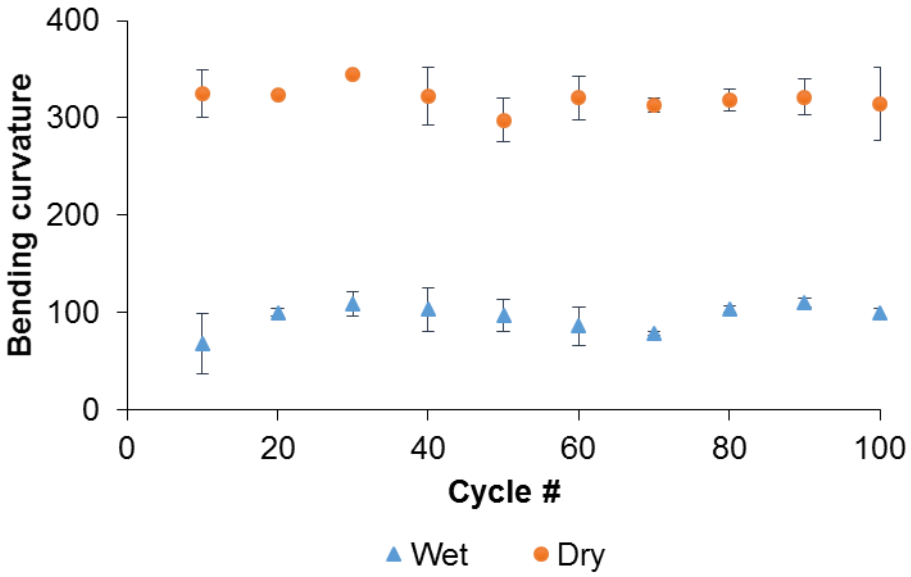

fig. S12. Sample stability test under 100 dry-wet cycles. Dry condition was performed by placing the samples on a hotplate for 5 seconds (50°C), while wet condition was performed by steaming for 5 seconds. The two conditions were switched back and force every 10 seconds. (**A**) Images of samples at representative dry-wet cycles. The number indicate the cycle times. (**B**) Quantitative measurement of the sample bending behaviors at dry-wet cycles.

table S1. Sequence of the synthetic gene used in this study.

Synthetic Gene	Sequence
eGFP	atgagcaagggcgaggagctgttcaccggggtggtgcccatcctggtcgagctggacggcgac gtaaacggccacaagttcagcgtgtccggcgagggcgagggcgatgccacctacggcaagctg accctgaagttcatctgcaccaccggcaagctgcccgtgccctggcccaccctcgtgaccaccct gacctacggcgtgcagtgcttcagccgctaccccgaccacatgaagcagcacgacttcttcaagtc cgccatgcccgaaggctacgtccaggagcgcaccatcttcttcaaggacgacggcaactacaag acccgcgccgaggtgaagttcgagggcgacaccctggtgaaccgcatcgagctgaagggcatc gacttcaaggaggacggcaacatcctggggcacaagctggagtacaactacaacagccacaac gtctatatcatggccgacaagcagaagaacggcatcaaggtgaacttcaagatccgccacaacat cgaggacggcagcgtgcagctcgccgaccactaccagcagaacaccccccatcggcgacggcc ccgtgctgctgcccgacaaccactacctgagcacccagtccgccctgagcaaagaccccaacga gaagcgcgatcacatggtcctgctggagttcgtgaccgccgccgggatcactctcggcatggacg agctgtacaagtaa

movie S1. Biohybrid bilayer film at different RHs.

movie S2. Single-cell volume change when decreasing RH imaged by dark-field microscopy.

movie S3. Fluorescence change of biohybrid film at different RHs.

movie S4. Simulation of bilayer biofilm bending.

movie S5. Simulation of sandwich-structured biofilm bending.

movie S6. Flaps opening for garment during exercise.